Landslides (2018) 15:1991–2000
DOI 10.1007/s10346-018-0999-8
Received: 8 August 2017
Accepted: 27 April 2018
Published online: 12 May 2018

Xavi Gallach · Ludovic Ravanel · Markus Egli · Dagmar Brandova · Michael Schaepman · Marcus Christl · Stephan Gruber · Philip Deline · Julien Carcaillet · François Pallandre

Timing of rockfalls in the Mont Blanc massif (Western Alps): evidence from surface exposure dating with cosmogenic ^{10}Be

Abstract Rockfalls and rock avalanches are a recurrent process in high mountain areas like the Mont Blanc massif. These processes are surveyed due to the hazard they present for infrastructure and alpinists. While rockfalls and rock avalanches have been documented for the last 150 years, we know very little about their frequency since the Last Glacial Maximum (LGM). In order to improve our understanding, it is imperative to date them on a longer timescale. A pilot campaign using Terrestrial Cosmogenic Nuclide (TCN) dating of five samples was carried out in 2006 at the Aiguille du Midi (3842 m a.s.l.). In 2011, a larger scale study (20 samples) was carried out in five other test sites in the Mont Blanc massif. This paper presents the exposure ages of the 2011 TCN study as well as the updated exposure ages of the 2006 study using newer TCN dating parameters. Most of these exposure ages lie within the Holocene but three ages are Pleistocene (59.87 ± 6.10 ka for the oldest). A comparison of these ages with air temperature and glacier cover proxies explored the possible relationship between the most active rockfall periods and the warmest periods of the Holocene: two clusters of exposure ages have been detected, corresponding to the Middle Holocene (8.2–4.2 ka) and the Roman Warm Period (c. 2 ka) climate periods. Some recent rockfalls have also been dated (< 0.56 ka).

Keywords ^{10}Be cosmogenic nuclide dating · Rockfalls · Late-glacial · Holocene · Mont Blanc massif

Introduction

Present-day rockfalls (> 100 m^3) and rock avalanches (> 10^5 m^3) in the Mont Blanc Massif (MBM) are surveyed and documented by a network of observers (hut keepers, mountain guides, alpinists) operational since 2007 (Ravanel et al. 2010a; Ravanel and Deline 2013). A clear relationship between the hottest periods of the year and a high frequency of rockfall has been established, especially during the hot summers of 2003 and 2015, very likely caused by permafrost degradation due to current climate change (Schiermeier 2003; Gruber et al. 2004; Ravanel et al. 2017). This relationship has also been proposed when studying rockfall occurrence in other regions of the Alps (Fischer et al. 2012; Luethi et al. 2015) and in other distant regions as the New Zealand Southern Alps (Allen et al. 2009).

Rockfall frequency in the MBM over the past 150 years has been studied by comparing historical photographs (Ravanel 2010; Ravanel and Deline 2008, 2010). Since 1860, more than 70% of rockfalls in the study areas have occurred during the last three decades. Since the end of the nineteenth century, air temperature in the European Alps has risen by an average of 2 °C, with an increase of 1.2 °C between 1988 and 2003 (Auer et al. 2007). Resulting permafrost warming and active layer deepening has increased the frequency of rockfalls (Ravanel et al. 2017).

On a longer timescale, landslide frequency during the Holocene has been widely studied in the Alps (Soldati et al. 2004; Zerathe et al. 2014; Ivy-Ochs et al. 2017) and worldwide (Ballantyne 2008; Ballantyne et al. 1998; Hermanns et al. 2004; Mercier et al. 2013). In the Alps, landslide ages obtained by various dating methods show three clusters of events at 10–9, 5–3 and < 2 ka. Early Holocene landslides are generally related to postglacial debuttressing, while Middle and Late Holocene events are generally related to climate change (heavy rainfall).

However, in order to understand rockfall frequency during both Late-glacial and Holocene periods, both of which have been poorly studied and documented, we need more widespread sampling. TCN dating of large rock wall scars provides useful data which will enable us to trace their occurrence back to the post-LGM period, and a possible relationship with warmer climate periods.

Rockfall frequency and a potential relation to climate variability can only then be obtained when a dataset covering a large time range is available. A first hint of the age of a rockfall can be retrieved from the colour of the rock surface. Rock surfaces recently exposed by rockfalls are evidenced by both light grey colour (Ravanel and Deline 2008) and broken rock bridges. As weathering of the biotite (the main ferromagnesian mineral in the MBM granite) produces iron oxide, percolation on rock walls surfaces causes a typical orange-reddish colour. Böhlert et al. (2008) showed in a preliminary study that the redness of the granite surface in the MBM seems time-dependent (the redder a rock surface is, the longer it has been exposed to weathering). We therefore tried to assess rockfall intensities over a largest possible timescale using the approach of surface redness as first indication.

In order to assure the broadest possible range of exposure ages, we aimed to sample the widest colour range at each site, avoiding areas presumably glaciated since the LGM in order to avoid collecting data which has resulted from the addition of successive exposure ages.

Mont Blanc massif and the test sites

The MBM (Fig. 1) extends over 550 km^2 on the outer margin of the Western Alps. Glaciers cover the 27% of its surface area and continuous permafrost is present in at least 39 km^2 of rock walls steeper than 40° (Magnin et al. 2015).

Almost all MBM rocks are crystalline, the Late-Hercynian granite being intrusive in a Hercynian metamorphic series. These rocks show evidence of a multiphase geological history, which generated shear zones and fractures (Rossi 2005). The large-scale deformation that affects Mont Blanc granite corresponds to faults and shear zones. Superimposed Hercynian and Alpine structures, mainly oriented N 0–25° E and N 45–60° E, respectively (Butler

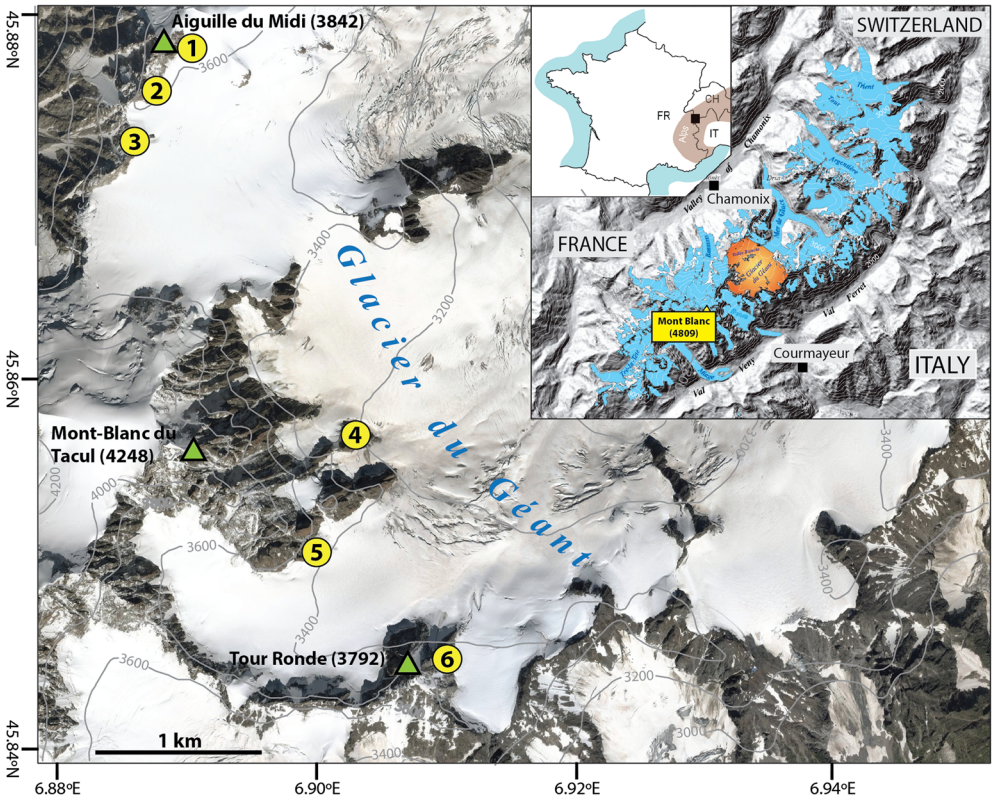

Fig. 1 Study sites in the Mont Blanc massif. 1, Aiguille du Midi; 2, Cosmiques Spur; 3, lower Cosmiques Ridge; 4, Pyramide du Tacul; 5, Trident du Tacul; 6, Tour Ronde. Elevation in meters a.s.l.

1985), are highlighted by more or less continuous mylonitic zones on which the morphology of the massif partly depends. At the outcrop-scale, the deformation mainly concords with the major fracture lines. Strike of the main joint families follows the predominant fault-line. Joints and slope steepness make the MBM conducive to both rockfalls and rock avalanches (Deline et al. 2012). For instance, the Brenva Glacier basin experienced ice-rock avalanches in both 1920 and 1997, the rock volume of which was *c.* 3×10^6 m^3 and 2×10^6 m^3, respectively (Deline et al. 2015).

The six rock walls sampled in 2011 are located in the Glacier du Géant basin, in the central part of the MBM (Figs. 1 and 2). The most northerly (Aiguille du Midi) and southerly (Tour Ronde, on the crest line between France and Italy) sampling sites are 4.2 km apart; elevation is in the range 3300–3800 m a.s.l. (Table 1).

Methods

Sampling locations

Sampling was carried out in September 2011, mostly on E and SE faces, where the transition from grey (corresponding to fresh rock) to orange/red colour was most obvious. Nineteen surfaces of different redness, exposed N 45° to N 180°, and one surface exposed N 270°, were selected at six sites at elevations in the range of 3355 to 3825 m a.s.l. The aim was to cover the broadest possible range of surface redness and rockfall ages. Sampling was carried out in such a way as to avoid areas where the colour was too different from its overall aspect (joints, roofs). Both surface exposure dating and reflectance spectroscopy were carried out on each sample.

The different colour units at the six selected sites were determined from photographs and field work. Based on these observations, the rock wall surfaces were classified according to their apparent exposure age (Fig. 2): T1 (older) to T4 (younger).

The Aiguille du Midi (Fig. 2a, c), was sampled at the top of the SE Pillar (T1), where the very dark orange surface suggests that it should be the oldest exposed rock; (ii) ADM8 comes from a light grey rockfall scar in the W face of the Central Pillar (T3), suggesting a lower exposure age.

The Cosmiques Spur (Fig. 2a) is a rock wall characterised in its lower section by a long roof formed by rockfalls. The upper half (T2) has the orange colour typical of the surrounding zones while the lower half (T1) presents two sections with a dark orange surface, likely due to water along a fracture within the rock mass before rockfall that corroded Fe. The central section of the lower half (T3) is a rockfall scar having a lighter colour.

The lower Cosmiques Ridge is where the Cosmiques hut is located (3613 m a.s.l.; Fig. 2b). The part of the rock wall below the hut (T3) has a light grey colour and was exposed recently by the lowering of the glacier surface (Ravanel et al. 2013). COS1 was sampled within the scar of a 1998 rockfall (T4; Ravanel et al. 2013), to check the accuracy of the TCN inventory on a very young dated surface.

On the Pyramide du Tacul (Fig. 2d), a large scar (T3) spans the SE and NE faces giving a slabby, grey depression. The small colour difference between the darker T1 and lighter T2 zones is not sufficient for us to consider T2 a rockfall scar.

On the steep SE and E faces of the Trident du Tacul (Fig. 2e), the very steep and indented summit pillars (T1) are the reddest;

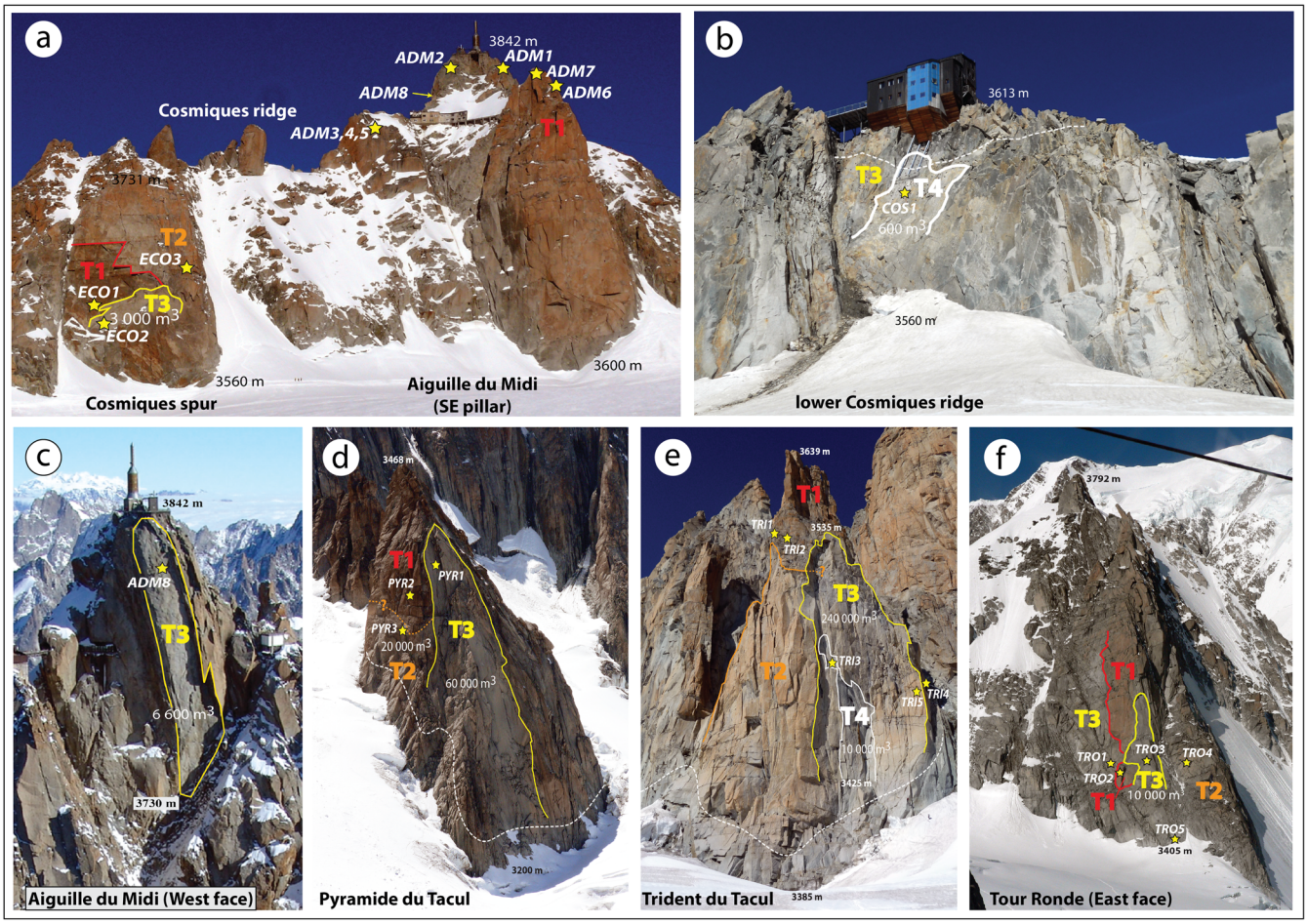

Fig. 2 Sampling sites in the Mont Blanc massif. T1 to T4: oldest to youngest areas of rock as estimated prior to sampling; white dotted line: trimline showing glacier shrinkage since the 1980s

they tower above a less steep and fractured sector which is delimited at its lower edge by large overhangs. Further down, the SE face is an orange scar with several ribs and cracks. The E face (T3) is a large scar varying in colour from orange in the lower east section to light grey. Finally, a more recent rockfall scar has a light grey colour (T4)—which is lighter still at its recently deglaciated base.

The main rock wall of the E face of the Tour Ronde (Fig. 2f) is separated by a dihedral from a secondary rock wall (T2). The main rock wall has a dark orange, vertical, central part (T1), abutting an upper grey zone (T3); a grey rockfall scar is located in the lower part (T3). Finally, the lightest grey corresponds to the recently deglaciated area at the bottom of the face.

Sampling protocol

Sampling was carried out as follows: (i) access to the summit of each selected rock wall by cable car and walking (Aiguille du Midi, Cosmiques Spur, lower Cosmiques Ridge) or by helicopter (Pyramide du Tacul, Trident du Tacul, Tour Ronde); (ii) fix static ropes down the zone to be sampled; (iii) search for a fragile zone to facilitate the sampling and optimise logistics; (iv) drill closely spaced intersecting holes with a cordless percussion drill and (v) extract the rock sample with a chisel and hammer. Each sample is composed of one to four pieces of rock (Fig. 3); sample thickness is up to 6.5 cm, with a sample mass in the range 1.15–4.60 kg (mean 2.50 kg). Sampling was carried out in > 3 m-deep rockfall scars to avoid cosmogenic nuclides inheritance, as ~ 99% of cosmic rays are absorbed in the first 3 m of granite (Dunai 2010).

Sample processing

Approximately 1 kg of each rock sample was crushed and sieved to obtain a grain-size of 0.25–0.5 mm. The samples were then leached in order to obtain pure quartz (Kohl and Nishiizumi 1992; Ivy-Ochs 1996). After atmospheric ^{10}Be decontamination (by 3 sequential HF leaching), ^{9}Be carrier solution was added and the sample was then dissolved in 40% HF. Be was isolated using anion and cation exchange columns followed by selective pH precipitation techniques (Brown et al. 1991; Merchel and Herpers 1999). The Be hydroxides were precipitated, dried, and calcined at 850 °C to BeO.

The ^{10}Be/^{9}Be ratios were measured at the ETH Zurich Tandem Accelerator Mass Spectrometry (AMS) facility (Kubik and Christl 2010). The ^{10}Be concentrations were corrected for ^{10}Be in the ^{9}Be carrier solution ($1.68 \pm 0.20 \times 10^{-14}$) and normalised to the ETH secondary standard S2007 N with a nominal value of ^{10}Be/^{9}Be = 28.1×10^{-12}. S2007 N was calibrated with a primary standard ICN 01–5-1 (Nishiizumi et al. 2007) and has a nominal value of 2.709×10^{-11}. The 1σ error of S2007 N is 2.7%.

Table 1 Main characteristics of the sampling sites

Study site	Alt. min. (m a.s.l.)	Alt. max. (m a.s.l.)	Lat. (°N)	Long. (°E)	Average slope (°)	Sample	Unit	Altitude (m a.s.l.)	Slope (°)	Aspect (°N)	Scar-corresponding rockfall volume (m^3)[4]
Aiguille du Midi	3600	3842	45.8787	6.8878	60	ADM1[1]	T1	3821	85	165	-
						ADM2[1]	T2	3825	85	138	-
						ADM3[1]	T2	3750	49	135	-
						ADM4[1]	T2	3740	79	127	-
						ADM5[1]	T2	3740	79	149	-
						ADM6	T1	3780	82	142	–
						ADM7	T1	3790	76	162	–
						ADM8	T3	3815	86	270	6600
Lower Cosmiques ridge	3560	3613	45.8732	6.8858	65	COS1	T4	3593	63	125	600
Cosmiques spur	3560	3731	45.8761	6.8870	75	ECO1	T1	3625	72	142	6400
						ECO2	T3	3600	83	140	3000
						ECO3	T2	3627	69	132	–
Pyramide du Tacul	3200	3468	45.8564	6.9022	70	PYR1	T3	3400	62	136	60,000
						PYR2	T1	3380	85	136	–
						PYR3	T2	3355	68	140	20,000
Trident du Tacul	3385	3639	45.8509	6.8997	85	TRI1	T1	3526	88	148	–
						TRI2[2]	T1	3523	72	105	–
						TRI3	T4	3471	90	105	10,000
						TRI4	T1	3464	86	48	–
						TRI5	T3	3460	90	145	240,000
Tour Ronde East face	3405	3792	45.8448	6.9095	80	TRO1	T3	3445	83	112	–
						TRO2	T1	3430	85	135	–
						TRO3	T3	3440	85	90	10,000
						TRO4	T2	3440	74	105	–
						TRO5[3]	T4	3410	81	89	–

[1] Böhlert et al. (2008)

[2] Sample showing strong desquamation of minerals

[3] Sample taken only a few meters above the current glacier surface

[4] Rockfall volumes are proposed for the best preserved rockfall scars, where volume can be estimated using 3D reconstructing techniques

Fig. 3 Samples for TCN dating (a-axis × b-axis, in cm), and final stage of the extraction of a sample (ADM7)

The exposure ages were calculated with *The online calculators formerly known as the CRONUS-Earth online calculators* (Balco et al. 2008; http://hess.ess.washington.edu/math/).

The production rate was scaled for latitude and altitude based on Stone (2000) and corrected for sample thickness assuming an exponential depth profile (Brown et al. 1992) with an effective neutron attenuation length of 160 g cm^{-2} (Gosse and Phillips 2001) and a rock density of 2.65 g cm^{-3}. Geomagnetic field correction was omitted (Masarik et al. 2001; Pigati and Lifton 2004) because the effect is small in the Alps (max. 1–2%). A ^{10}Be half-life of 1.39 Myr (Chmeleff et al. 2010; Korschinek et al. 2010) was used for the calculation of exposure ages. The shielding of the surrounding topography (based on Dunne et al. 1999) was taken into consideration (Table 2). No correction for snow was applied. We calculated the ages using an erosion rate of 1 mm/ky.

Exposure age obtained from one sample in a rockfall scar is considered as the minimum time since the last rockfall. Since both erosion and snow cover are considered negligible, in the absence of surface dissolution and frost shattering (highly fractured areas were avoided), and due to sub-vertical rock walls, the minimum exposure age can be considered the true exposure age.

Rockfall volumes

In order to estimate detached rock volumes, scars at the Pyramide and the Trident du Tacul were measured using a Laser Technology TruPulse 200 laser range finder with inclinometer (effective range 500 m, accuracy ± 30 cm and ± 0.25°; Ravanel and Deline 2010). Rock walls at the four other study sites were surveyed with an Optech ILRIS 3D terrestrial laser scanner (effective range 600 m; Ravanel et al. 2010b), and a 3D model was produced for every rock wall. Rockfall volumes were calculated for the most evident scars, as a quantification of the difference existing between the current rock wall surface and the estimated surface shape prior to collapse. Uncertainty in the calculation of rockfall volumes can reach up to 1/3 of the volume, specially in those scars offering few clues to reconstruct a collapsed surface. But this does not affect the analysis of the rockfall frequency which is the main aim of this work.

Results

Twenty samples were dated in the 2011 survey, and the five dates of the 2006 survey were recalculated using current standards (Table 2). Six samples failed to provide an exposure age due to technical problems (and there was not enough material for a second trial). All results can slightly be biased by inherited ^{10}Be. Consequently, the age of the surface prior to the rockfall had to be estimated (Table 2). Half of the sampling sites were covered by a glacier during the last glacial period. For the sites that were not covered, an exposure age of > 100 ka had to be assumed. The depth function and penetration of ^{10}Be into the rock was determined according to Hidy et al. (2010). The potential error

Table 2 Results of the ^{10}Be measurements. Shielding correction includes the effects caused by mountain topography, dip and strike of the various rock surfaces. Rock density is 2.7 g/cm^3. The exposure ages were calculated using an erosion rate of 1 mm/ka. The exposure of the surface prior to rockfall had to be estimated to calculate the inherited ^{10}Be content at 3 m-rock depth (sample location). Single dates are given in ^{10}Be-ka in order to allow straightforward correction for future refinements in scaling schemes and production rate computation

Sample	^{10}Be (10^4 at g^{-1})	Sample thickness (cm)	Shielding factor	Production rate (spallation) (at g^{-1} a^{-1})	Production rate (muons) (at g^{-1} a^{-1})	Exposure age (ka)	External uncertainty (± ka)	Estimated age of surfaces prior to rock fall (ka)	Estimated ^{10}Be content in 3 m depth (with shielding) (10^4 at g^{-1})	Corrected ^{10}Be content (10^4 at g^{-1})	Corrected surface age (of rock fall) (ka)	External uncertainty (± ka)
ADM1	157.63	2.5	0.559	33.67	0.241	46.62	4.44	> 100	1.9565	155.67	46.01	4.39
ADM2	6.03	3.5	0.559	33.58	0.241	1.71	0.22	15	0.1789	5.85	1.66	0.21
ADM3	24.28	5.5	0.898	51.36	0.235	4.53	0.45	15	0.4310	23.85	4.45	0.44
ADM4	24.84	2.5	0.627	36.55	0.238	6.48	0.63	15	0.2132	24.63	6.43	0.63
ADM5	28.28	4	0.627	36.1	0.236	7.49	0.75	15	0.213 s	28.07	7.43	0.75
ADM6	–	–	–	–	–	–	–	–	–	–	–	–
ADM7	–	–	–	–	–	–	–	–	–	–	–	–
ADM8	1.05	4	0.529	35.94	0.584	0.32	0.06	> 100	1.1003	0	Recent	
COS1	0.17	1.2	0.791	45.67	0.545	0.04	0.02	15	0.3401	0	Recent	
ECO1	–	–	–	–	–	–	–	–	–	–	–	–
ECO2	1.8	6	0.582	33.74	0.547	0.57	0.10	15	0.1862	1.61	0.51	0.10
ECO3	21.3	6.5	0.734	43.05	0.544	5.28	0.67	15	0.3009	20.99	5.22	0.67
PYR1	–	–	–	–	–	–	–	–	–	–	–	–
PYR2	154.15	5	0.559	28.85	0.517	60.49	6.15	> 100	1.6826	152.47	59.87	6.10
PYR3	9.01	3	0.743	36.62	0.518	2.50	0.33	15	0.2601	8.75	2.43	0.32
TRI1	21.18	4	0.523	29.66	0.536	7.65	0.96	>100	1.5114	19.67	7.11	0.93
TRI2	51.69	2.5	0.703	40.45	0.54	13.86	1.30	>100	2.7487	48.94	13.13	1.25
TRI3	–	–	–	–	–	–	–	–	–	–	–	–
TRI4	5.86	3.5	0.547	29.32	0.523	2.08	0.25	15	0.1532	5.71	2.03	0.24
TRI5	16.04	5.5	0.5	23.56	0.513	6.36	0.64	15	0.1150	15.93	6.32	0.63
TRO1	1.4	4	0.582	31.45	0.533	0.47	0.08	15	0.1746	1.23	0.41	0.08
TRO2	11.95	4	0.559	30.18	0.532	4.16	0.42	15	0.1621	11.79	4.11	0.42
TRO3	–	–	–	–	–	–	–	–	–	–	–	–
TRO4	6.75	4.5	0.682	35.91	0.532	1.96	0.36	15	0.2319	6.52	1.90	0.35
TRO5	0.37	7	0.605	32.26	0.52	0.13	0.03	15	0.1876	0.18	0.06	0.03

Ages of samples ADM1 to ADM5 corrected in 2018; original dates have been published in Böhlert et al. (2008)

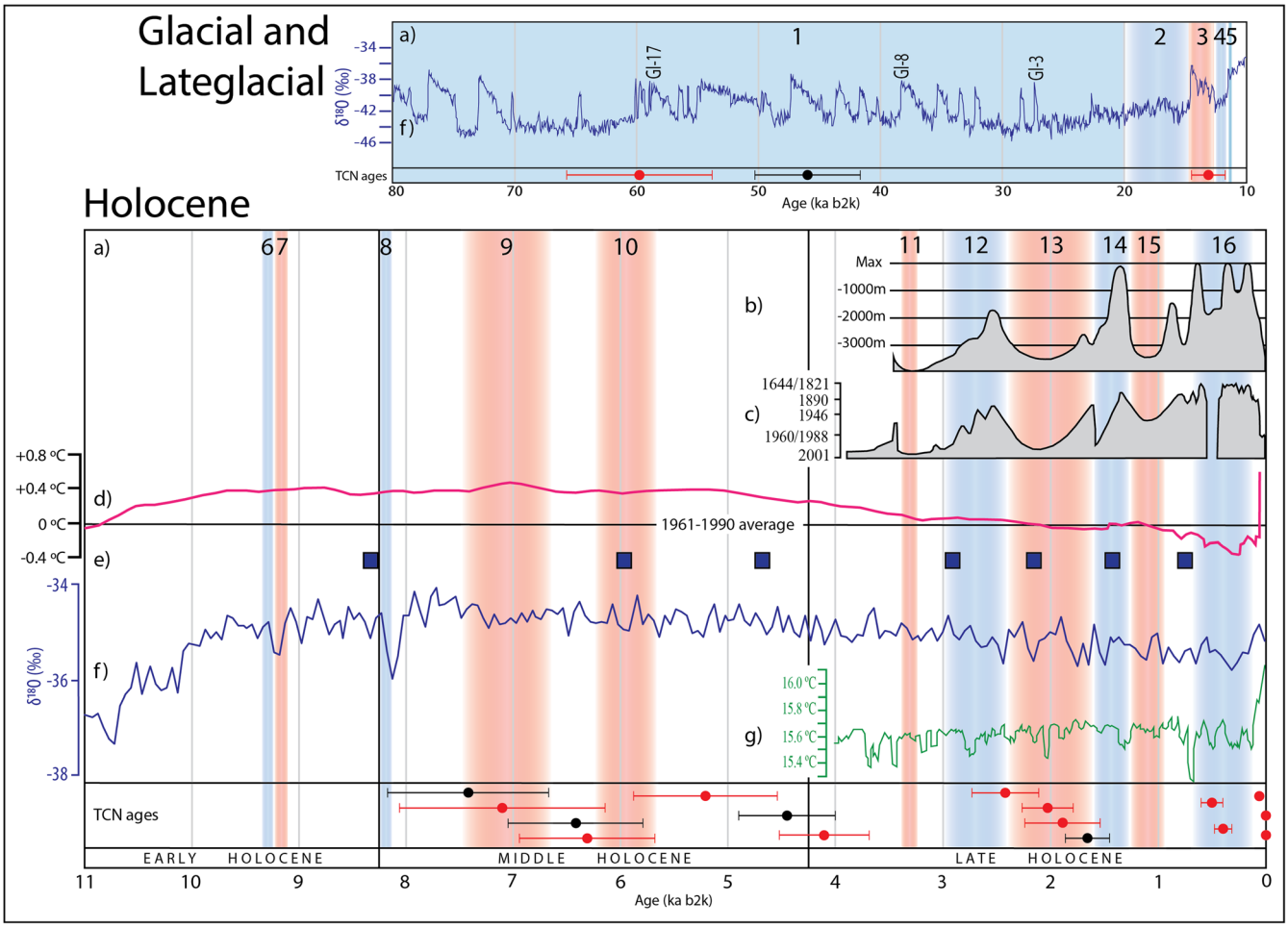

Fig. 4 Results from TCN dating of rockfalls (black: 2006 survey, Böhlert et al. 2008; red: 2011 survey, this study) and climate/glacier proxies during the Holocene and the last 80 ka (insert). Early-Middle-Late Holocene divisions after Walker et al. (2012). GI, Glacial Interstadials (Svensson et al. 2008). (a) Climate events: 1, Last Glacial period; 2, Late-glacial; 3, Allerød oscillation; 4, Younger Dryas (Ivy-Ochs et al. 2009); 5, Preboreal oscillation (Rasmussen et al. 2007); 6, 9.3 ka cold event (Rasmussen et al. 2007); 7,9,10, Holocene warm intervals (Joerin et al. 2008); 8: 8.2 ka cold event (NGRIP members 2004); 11, Bronze Age Optimum; 12, Göschener I Cold stage (Zoller et al. 1966); 13, Roman Warm Period (Haas et al. 1998); 14, Göschener II Cold stage (Zoller et al. 1966); 15, Medieval Warm Period; 16, Little Ice Age (Mann 2002); (b) distance of Aletsch Glacier front to maximal Holocene advance (Holzhauser et al. 2005); (c) altitudinal variation of the Mer de Glace surface (Le Roy et al. 2015); (d) global mean temperature anomaly (Marcott et al. 2013); (e) ice-rafting events in the North Atlantic (Bond 1997); (f) NGRIP oxygen isotopic profile (NGRIP members 2004); (g) modelled North Hemisphere temperature (Kobashi et al. 2013)

introduced by inherited ^{10}Be is however, only marginal (Table 2). The resulting exposure ages range from recent to 59.87 ± 6.10 ka, and fall mostly into the Holocene period (except those for ADM1, PYR2 and TRI2). The age of three large rockfalls (10,000–60,000 m^3) remains unknown because PYR1, TRI3 and TRO3 could not be dated (Table 2).

The youngest exposure ages (< 1 ka: ADM8, COS1, ECO2, TRO1, and TRO5) were all sampled in grey to light orange scars. COS1 gave an age of 0 (recent) for the 1998 scar (Ravanel et al. 2013), which is very good considering the potential errors due to ^{10}Be inheritance and measurements errors of the AMS. All orange to dark orange rock surfaces showed ages > 1 ka, in the range 1.66 ± 0.21 ka (ADM2) to 59.87 ± 6.10 ka (PYR2). These findings generally confirm the hypothesis that *the redder the surface, the older its age* (Böhlert et al. 2008). The light orange TRI2 having an age of 13.13 ± 1.25 ka is considered as an outlier because of either a strong desquamation of minerals on its surface that could have prevented the development of a darker colour, or a recent surficial exfoliation. The time needed for the granite of the MBM's high-altitude rock walls to turn from light grey to orange is at least several hundred years, as seen when comparing the rock surface colour with its surface exposure age. Special consideration should be given to ADM8, the only west-exposed sample: since the walls exposed east, north and west are colder than south-exposed walls, weathering process are slower, therefore the orange colour is in general less developed in those aspects.

Discussion

The five youngest exposure ages (< 0.51 ka), occurred during and after the Little Ice Age (Fig. 4, climate event 16). Among these, three ages correspond to three well preserved rockfall scars, with 3D model-calculated volumes of 600 m^3 (COS1), 3000 m^3 (ECO2) and 6600 m^3 (ADM8). Regardless of lithology and geometry of pre-existing fracture patterns, rockfall volumes follow a recurrent

power law distribution (Dussauge et al. 2003). The analysis of 640 rockfalls in the MBM, mainly surveyed by the observer network (Ravanel and Deline 2013) in 2003 and 2007–2015, gave rise to a similar power law distribution for rockfall volumes between 300 and 15,000 m^3 (unpublished data). According to this dataset, these three rockfall volumes correspond to typical low magnitude/high frequency rockfalls that take place almost every year: 3 times/year for 600 m^3 rockfalls, 0.6 times/year for 3000 m^3 rockfalls and 0.3 times/year for 6600 m^3 rockfalls. If such events happened today, they would be considered within the "regular" magnitude and frequency. The two other LIA/post-LIA ages correspond to a recently deglaciated area (TRO5) and a fractured zone (TRO1).

A cluster of four ages (1.7–2.4 ka) is consistent with the Roman Warm Period (Haas et al. 1998; Fig. 4, climate event 13), during which temperatures were higher and several glaciers in the western Alps retreated very significantly (Hormes et al. 2006; Ivy-Ochs et al. 2009; Le Roy et al. 2015; Fig. 4). Warming of the MBM permafrost could have affected rock wall stability and led to an increase in collapses (Magnin et al. 2017; Ravanel et al. 2017).

A second cluster of seven ages (4.1–7.4 ka) corresponds to the Middle Holocene (MH, 8.2–4.2 ka; Walker et al. 2012, Fig. 4) that started after the 8.2 ka cold event. The MH climate was highly variable (Mayewski et al. 2004), it became the warmest period of the Holocene (Baroni and Orombelli 1996; Joerin et al. 2008; Nicolussi 2009; Le Roy 2012), and there is general agreement that the Northern Hemisphere became drier and warmer than during the Early Holocene (NGRIP members 2004). As already suggested by Le Roux et al. (2009), the MH appears to be favourable to rockfall triggering.

Among the exposure ages considered in this study, two are older than the Holocene (ADM1, 46.01 ± 4.39 ka; PYR2, 59.87 ± 6.10 ka) and fall into the Last Glacial period. Owing to their rather large error range, these dates cannot be directly be related to a specific Glacial Interstadial.

The samples dating from the Last Glacial period were located > 100 m above the current glacier level (Fig. 2). These zones were very probably not covered by the glacier during the LGM, because the glacier surface was only approximately 40–60 m above the current level (Coutterand and Buoncristiani 2006). The lack of ages older than 10 ka at the bottom of the rock walls, however, suggests that these areas were covered by the glacier and that their deglaciation enabled rockfall triggering, as confirmed by the Holocene ages.

Big rockfall scars could be attributed to a sequence of multiple events. However, a sequence of rockfalls is generally composed of very few major events and several minor events (Ravanel and Deline 2008), and lasts few hundreds of years. When studying holocene rockfalls, we assume that the duration of any potential rockfall sequence fits within the uncertainty of its corresponding TCN age. Therefore, we consider that our TCN ages are representative of the rockfalls ages.

Trident du Tacul T3 (Fig. 2e) is the largest rockfall scar (240,000 m^3) investigated in this study. It was partly below the likely LGM glacier level. TRI5, in the reddest area of T3, shows an age of 6.32 ± 0.63 ka. The lighter orange and grey areas within T3 suggest a complex rockfall history that started ~ 7 ka ago in the deglaciated area at the bottom of the rock wall.

Glacial erosion at the base of rock walls located in the accumulation zone is very low due to glacial flux being directed away from the wall towards the center of the valley (Paterson 1994). Glacial debuttressing and rock stress redistribution in these zones are also likely to be negligible as glacier shrinkage is reduced in the accumulation zone (McColl 2012). A main trigger for rockfall during the warmest periods of Late-glacial and Holocene could have been the cryostatic pressure from ice segregation (Murton et al. 2006) combined with hydrostatic pressure in ice-filled joints (Krautblatter et al. 2013). Part of the cause of these rockfalls could also be the degradation of the permafrost that formed when glacier surfaces became lower exposing the base of the rock wall to cold air (Wegmann et al. 1998). Through the deepening of the active layer, the permafrost degradation causes small volume rockfalls (a few hundred to thousands of m^3) and rather quickly, for example in connection with a hot summer (Ravanel et al. 2017). On the other hand, large rockfalls are staggered in time for several years or decades and involve permafrost degradation in depth (Gruber and Haeberli 2007).

Previous studies have explored the timing of Late-glacial and Holocene landslides and their relationship with climate. However, these landslides did not occur in high mountain environments. Soldati et al. (2004) suggest there have been two clusters of landslide periods in the Italian Dolomites, one at 11.5–8.5 ka and the other at 5.8–2 ka. The first seems to have been triggered by postglacial decompression and the second by a period of increased precipitation. Exposure ages of dated landslides in mudstone and limestone subalpine chains (Zerathe et al. 2014) are concentrated at *c.* 9.5 and 4.2 ka, periods that are characterised by heavy rainfall. Ivy-Ochs et al. (2017) see two main clusters of landslide activity since the end of the LGM: one around 10–9 ka that coincides with a rapid warming at 10.5–10 ka, and another around 5–3 ka. Some landslides also occurred during the Late-glacial period between 15.6 and 12.6 ka. It is known that strong earthquakes can also trigger rockfalls. Large palaeo-earthquakes occurred in central Switzerland about 2.2, 11.6 and 13.8 ka BP (Strasser et al. 2006). If or to which extent such earthquakes affected the Aiguille du Midi region is unknown, but the measured dates around 13.1 and 2.2 ka BP would fit with these events.

The relationship between climate and landslide triggering needs to be better established. Our results regarding the timing of rockfalls on high-altitude walls in the Mont Blanc massif only allow us to establish two possible time-clusters (1.7–2.4, 4.1–7.4 ka). These do not match the above-mentioned clusters of landslides. This is not unexpected due to differences in processes and environments.

Conclusion

TCN dating enabled to give an idea of rockfall frequency of the MBM over a large timescale. Dating complements historical evidence such as photograph datasets and present-day observations and surveys. Dating of rockfall surfaces always has the bias that the inherited ^{10}Be content is not really known and has to be estimated. If the samples are taken deep enough in rockfall scars, then this problem is strongly reduced. We showed that the introduced error was in our case very small.

The dataset presented here is still not yet sufficient enough to establish a clear relationship between the main rockfall episodes and climate, e.g., the warmest periods of the Holocene and the Late-glacial. So far we do not have exposure ages for the Bronze Age climate optimum that was characterised by higher

temperatures and stronger glacial recession than the Roman Warm Period. Furthermore, climate is not the only trigger mechanisms of rockfalls. To better disentangle such processes, a broader dataset is needed. Nonetheless, we demonstrate that a significant part of the occurred rockfalls correlate well with climate variability. The youngest rockfall events occurred during and after the Little Ice Age. A second cluster is consistent with the Roman Warm Period and a third cluster corresponds to the Middle Holocene (climate optimum).

Acknowledgments

This study is part of ANR 14-CE03-0006 *VIP Mont Blanc*, ALCOTRA 342 *PrévRisk Haute Montagne* and Alpes Grenoble Innovation Recherche *RED Mont-Blanc* projects. We thank three anonymous reviewers for their constructive criticism that helped to improve the paper.

References

Allen SK, Gruber S, Owens IF (2009) Exploring steep bedrock permafrost and its relationship with recent slope failures in the Southern Alps of New Zealand. Permafr Periglac Process 20:345–356. https://doi.org/10.1002/ppp.658

Auer I, Böhm R, Jurkovic A, Lipa W, Orlik A, Potzmann R, Schöner W, Ungersböck M, Matulla C, Briffa K, Jones P, Efthymiadis D, Brunetti M, Nanni T, Maugeri M, Mercalli L, Mestre O, Moisselin JM, Begert M, Müller-Westermeier G, Kveton V, Bochnicek O, Stastny P, Lapin M, Szalai S, Szentimrey T, Cegnar T, Dolinar M, Gajic-Capka M, Zaninovic K, Majstorovic Z, Nieplova E (2007) HISTALP-historical instrumental climatological surface time series of the Greater Alpine Region. Int J Climatol 27:17–46. https://doi.org/10.1002/joc.1377

Balco G, Stone JO, Lifton NA, Dunai TJ (2008) A complete and easily accessible means of calculating surface exposure ages or erosion rates from ^{10}Be and ^{26}Al measurements. Quat Geochronol 3:174–195

Ballantyne CK (2008) After the ice: Holocene geomorphic activity in the Scottish Highlands. Scott Geogr J 124(1):8–52

Ballantyne CK, Stone JO, Fifield LK (1998) Cosmogenic Cl-36 dating of postglacial landsliding at the Storr, Isle of Skye, Scotland. The Holocene 8:347–351

Baroni C, Orombelli G (1996) The Alpine 'Iceman' and Holocene climatic change. Quat Res 46:78–83

Böhlert R, Gruber S, Egli M, Maisch M, Brandová D, Haeberli W, Ivy-Ochs S, Christl M, Kubik P.W, Deline P (2008) Comparison of exposure ages and spectral properties of rock surfaces in steep, high alpine rock walls of Aiguille du Midi. Proceedings of the 9th International Conference on Permafrost, Institute of Northern Engineering–University of Alaska Fairbanks 143–148

Bond G (1997) A pervasive millennial-scale cycle in North Atlantic Holocene and glacial climates. Science 278:1257–1266. https://doi.org/10.1126/science.278.5341.1257

Brown ET, Edmond JM, Raisbeck GM, Yiou F, Kurz MD, Brook EJ (1991) Examination of surface exposure ages of Antarctic moraines using in-situ produced 10Be and 26Al. Geochim Cosmochim Acta 55:2269–2283

Brown E, Brook E, Raisbeck G, Yiou F, Kurz M (1992) Effective attenuation lengths of cosmic rays producing ^{10}Be and ^{26}Al in quartz: implications for exposure age dating. Geophys Res Lett 19:369–372

Butler RWH (1985) The restoration of thrust systems and displacement continuity around the Mont-Blanc massif, NW external Alpine thrust belt. J Struct Geol 7(5):569–582

Chmeleff J, von Blanckenburg F, Kossert K, Jakob D (2010) Determination of the ^{10}Be half-life by multicollector ICP-MS and liquid scintillation counting. Nucl Instrum Methods Phys Res Sect B: Bean Interact Mater Atoms, 268, Issue 2, 15, 192–199

Coutterand S, Buoncristiani J-F (2006) Paléogéographie du dernier maximum glaciaire du Pléistocène récent de la région du Massif du Mont Blanc, France. Quaternaire 17(1):35–43. https://doi.org/10.4000/quaternaire.633

Deline P, Gardent M, Magnin F, Ravanel L (2012) The morphodynamics of the Mont Blanc massif in a changing cryosphere: a comprehensive review. Geogr Ann: Ser A Phys Geogr 94:265–283

Deline P, Akçar N, Ivy-Ochs S, Kubik PW (2015) Repeated Holocene rock avalanches onto the Brenva Glacier, Mont Blanc massif, Italy: a chronology. Quat Sci Rev 126:186–200

Dunai TJ (2010) Cosmogenic nuclides principles, concepts and applications in the earth surface sciences. Cambridge University Press, Cambridge 187 p

Dunne J, Elmore D, Muzikar P (1999) Scaling factors for the rates of production of cosmogenic nuclides for geometric shielding and attenuation at depth on sloped surfaces. Geomorphology 27(1):3–11

Dussauge C, Grasso JR, Helmstetter A (2003) Statistical analysis of rockfall volume distributions: implications for rockfall dynamics. J Geophys Res: Solid Earth 108. https://doi.org/10.1029/2001JB000650

Fischer L, Purves RS, Huggel C, Noetzli J, Haeberli W (2012) On the influence of topographic, geological and cryospheric factors on rock slides and rockfalls in high mountain areas. Nat Hazards Earth Syst Sci 12:241–254. https://doi.org/10.5194/nhess-12-241-2012

Gosse JC, Phillips F (2001) Terrestrial in situ cosmogenic nuclides: theory and application. Quat Sci Rev 20:1475–1560

Gruber S, Haeberli W (2007) Permafrost in steep bedrock slopes and its temperature-related destabilization following climate change. J Geophys Res 112. https://doi.org/10.1029/2006JF000547

Gruber S, Hoelzle M, Haeberli W (2004) Permafrost thaw and destabilization of Alpine rock walls in the hot summer of 2003. Geophys Res Lett 31. https://doi.org/10.1029/2004GL020051

Haas JN, Richoz I, Tinner W, Wick L (1998) Synchronous Holocene climatic oscillations recorded on the Swiss Plateau and at timberline in the Alps. The Holocene 8:301–309

Hermanns R, Niedermann S, Ivy-Ochs S, Kubik P (2004) Rock avalanching into a landslide-dammed lake causing multiple dam failure in Las Conchas valley (NW Argentina)—evidence from surface exposure dating and stratigraphic analyses. Landslides 1:113–122. https://doi.org/10.1007/s10346-004-0013-5

Hidy AJ, Gosse JC, Pederson JL, Mattern JP, Finkel RC (2010) A geologically constrained Monte Carlo approach to modeling exposure ages from profiles of cosmogenic nuclides: an example from Lees Ferry, Arizona. Geochem Geophys Geosyst 11. https://doi.org/10.1029/2010GC003084

Holzhauser H, Magny MJ, Zumbühl HJ (2005) Glacier and lake-level variations in west-central Europe over the last 3500 years. The Holocene 15:789–801. https://doi.org/10.1191/0959683605hl853ra

Hormes A, Beer J, Schlüchter C (2006) A geochronological approach to understanding the role of solar activity on Holocene glacier length variability in the Swiss Alps. Geogr Ann Ser A, Phys Geogr 88:281–294

Ivy-Ochs S (1996) The dating of rock surfaces using in situ produced ^{10}Be, ^{26}Al and ^{36}Cl, with examples from Antarctica and the Swiss Alps. PhD Thesis, ETH Zürich, 196 p

Ivy-Ochs S, Kerschner H, Maisch M, Christl M, Kubik PW, Schlüchter C (2009) Latest Pleistocene and Holocene glacier variations in the European Alps. Quat Sci Rev 28:2137–2149

Ivy-Ochs S, Martin S, Campedel P, Hippe K, Alfimov V, Vockenhuber C, Andreotti E, Carugati G, Pasqual D, Rigo M, Vigano A (2017) Geomorphology and age of the Marocche di Dro rock avalanches (Trentino, Italy). Quat Sci Rev 169:188–205

Joerin UE, Nicolussi K, Fischer A, Stocker TF, Schlüchter C (2008) Holocene optimum events inferred from subglacial sediments at Tschierva Glacier, Eastern Swiss Alps. Quat Sci Rev 27:337–350. https://doi.org/10.1016/j.quascirev.2007.10.016

Kobashi T, Goto-Azuma K, Box JE, Gao CC, Nakaegawa T (2013) Causes of Greenland temperature variability over the past 4000 yr: implications for northern hemispheric temperature changes. Clim Past 9:2299–2317. https://doi.org/10.5194/cp-9-2299-2013

Kohl CP, Nishiizumi K (1992) Chemical isolation of quartz for measurement of in-situ-produced cosmogenic nuclides. Geochim Cosmochim Acta 56(9):3583–3587

Korschinek G, Bergmaier A, Faestermann T, Gerstmann UC, Remmert A (2010) A new value for the half-life of 10Be by heavy-ion elastic recoil detection and liquid scintillation counting. Nucl Instrum Methods Phys Res Sect B: Bean Interact Mater Atoms 268:187–191

Krautblatter M, Funk D, Günzel FK (2013) Why permafrost rocks become unstable: a rock–ice-mechanical model in time and space. Earth Surf Process Landf 38:876–887

Kubik PW, Christl M (2010) ^{10}Be and ^{26}Al measurements at the Zurich 6 MV tandem AMS facility. Nucl Instrum Methods B 268:880–883

Le Roux O, Schwartz S, Gamond JF, Jongmans D, Bourles D, Braucher R, Mahaney W, Carcaillet J, Leanni L (2009) CRE dating on the head scarp of a major landslide (Séchilienne, French Alps), age constraints on Holocene kinematics. Earth Planet Sci Lett 280:236–245. https://doi.org/10.1016/j.epsl.2009.01.034

Le Roy M (2012) Reconstitution des fluctuations glaciaires holocènes dans les Alpes occidentales - Apports de la dendrochronologie et des datations par isotopes cosmogéniques produits in situ (PhD thesis). Université de Grenoble

Le Roy M, Nicolussi K, Deline P, Astrade L, Edouard JL, Miramont C, Arnaud F (2015) Calendar-dated glacier variations in the western European Alps during the Neoglacial: the Mer de Glace record, Mont Blanc massif. Quat Sci Rev 108:1–22. https://doi.org/10.1016/j.quascirev.2014.10.033

Luethi R, Gruber S, Ravanel L (2015) Modelling of transient thermal conditions in rockfall detachment areas: towards a better understanding of failure mechanisms in a changing permafrost environment. Geogr Ann A 97(4):753–767. https://doi.org/10.1111/geoa.12114

Magnin F, Brenning A, Bodin X, Deline P, Ravanel L (2015) Modélisation statistique de la distribution du permafrost de paroi: application au massif du Mont Blanc. Géomorphologie: Relief, Process Environ 21:145–162. https://doi.org/10.4000/geomorphologie.10965

Magnin F, Josnin J-Y, Ravanel L, Pergaud J, Pohl B, Deline P (2017) Modelling rock wall permafrost degradation in the Mont Blanc massif from the LIA to the end of the 21st century. Cryosphere 11:1813–1834

Mann ME (2002) Little Ice Age. Encyclopedia of global environmental change. Volume 1, The Earth system: physical and chemical dimensions of global environmental change: 504–509

Marcott SA, Shakun JD, Clark PU, Mix AC (2013) A reconstruction of regional and global temperature for the past 11,300 years. Science 339:1198–1201

Masarik J, Frank M, Schäfer JM, Wieler R (2001) Correction of in situ cosmogenic nuclide production rates for geomagnetic field intensity variations during the past 800,000 years. Geochim Cosmochim Acta 65:2995–3003

Mayewski PA, Rohling EE, Curt Stager J, Karlén W, Maasch KA, Meeker LD, Meyerson EA, Gasse F, van Kreveld S, Holmgren K, Lee-Thorp J, Rosqvist G, Rack F, Staubwasser M, Schneider RR, Steig EJ (2004) Holocene climate variability. Quat Res 62:243–255. https://doi.org/10.1016/j.yqres.2004.07.001

Merchel S, Herpers U (1999) An update on radiochemical separation techniques for the determination of longlived radionuclides via accelerator mass spectrometry. Radiochim Acta 84:215–219

Mercier D, Cossart E, Decaulne A, Feuillet T, Jónsson HP, Sæmundsson Þ (2013) The Höfn ahólar rock avalanche (sturzström): chronological constraint of paraglacial landsliding on an Icelandic hillslope. The Holocene 23:432–446

Murton JB, Peterson R, Ozouf JC (2006) Bedrock fracture by ice segregation in cold regions. Science 314:1127–1129

McColl ST (2012) Paraglacial rock-slope stability. Geomorphology 153-154:1–16

Nicolussi K (2009) Klimaentwicklung in den Alpen während der letzten 7000 Jahre. Impulsreferate:109–124

NGRIP members (2004) High resolution record of Northern Hemisphere climateextending into the last interglacial period. Nature 431:147–151

Nishiizumi K, Imamura M, Caffee MW, Southon JR, Finkel RC, McAninch J (2007) Absolute calibration of ^{10}Be AMS standards. Nucl Instrum Methods Phys Res, Sect B 258:403–413. https://doi.org/10.1016/j.nimb.2007.01.297

Paterson WSB (1994) The physics of glaciers, 3rd edn. Elsevier Science, Tarrytown 480p

Pigati JS, Lifton NA (2004) Geomagnetic effects on time-integrated cosmogenic nuclide production with emphasis on in situ ^{14}C and ^{10}Be. Earth Planet Sci Lett 226:193–205. https://doi.org/10.1016/j.epsl.2004.07.031

Rasmussen SO, Vinther BM, Clausen HB, Andersen KK (2007) Early Holocene climate oscillations recorded in three Greenland ice cores. Quat Sci Rev 26:1907–1914. https://doi.org/10.1016/j.quascirev.2007.06.015

Ravanel L (2010) Caractérisation, facteurs et dynamiques des écroulements rocheux dans les parois à permafrost du massif du Mont-Blanc. PhD Thesis. Université de Savoie

Ravanel L, Deline P (2008) La face ouest des Drus (massif du Mont-Blanc) : évolution de l'instabilité d'une paroi rocheuse dans la haute montagne alpine depuis la fin du Petit Age Glaciaire. Géomorphologie: Relief, Process, Environ 4:261–272

Ravanel L, Deline P (2010) Climate influence on rockfalls in high-alpine steep rock walls: the north side of the Aiguilles de Chamonix (Mont Blanc massif) since the end of the Little Ice Age. The Holocene 21:357–365

Ravanel L, Deline P (2013) A network of observers in the Mont Blanc massif to study rockfalls in high alpine rock walls. Geogr Fis Din Quat 36:151–158. https://doi.org/10.4461/GFDQ.2013.36.12

Ravanel L, Allignol F, Deline P, Ravello M (2010a) Rock falls in the Mont Blanc massif in 2007 and 2008. Landslides 7:493–501. https://doi.org/10.1007/s10346-010-0206-z

Ravanel L, Deline P, Jaillet S (2010b) Quantification des éboulements/écroulements dans les parois de la haute montagne alpine: quatre années de laserscanning terrestre dans le massif du Mont-Blanc. Revue Française de Photogrammétrie et Télédétection 192:58–65

Ravanel L, Deline P, Lambiel C, Vincent C (2013) Instability of a highly vulnerable high alpine rock ridge: the lower Arête des Cosmiques (Mont Blanc massif, France). Geografiska Annaler: Series A, Phys Geogr 95(1):51–66

Ravanel L, Magnin F, Deline P (2017) Impacts of the 2003 and 2015 summer heat waves on permafrost-affected rock walls in the Mont Blanc massif. Sci Total Environ 609:132–143

Rossi M (2005) Déformation, transferts de matière et de fluide dans la croûte continentale: application aux massifs cristallins externes des Alpes. PhD Thesis, Université Joseph Fourier, 376 p

Schiermeier Q (2003) Alpine thaw breaks ice over permafrost's role. Nature 424:712

Soldati M, Corsini A, Pasuto A (2004) Landslides and climate change in the Italian dolomites since the Late glacial. Catena 55:141–161

Stone J (2000) Air pressure and cosmogenic isotope production. J Geophys Res 105:23753–23759

Strasser M, Anselmetti FS, Fäh D, Giardini D, Schnellmann M (2006) Magnitudes and source areas of large prehistoric northern Alpine earthquakes revealed by slope failures in lakes. Geology 34:1005–1008

Svensson A, Andersen KK, Bigler M, Clausen HB, Dahl-Jensen D, Davies SM, Johnsen SJ, Muscheler R, Parrenin F, Rasmussen SO, others (2008) A 60 000 year Greenland stratigraphic ice core chronology. Clim Past 4:47–57

Walker MJC, Berkelhammer M, Björck S, Cwynar LC, Fisher DA, Long AJ, Lowe JJ, Newnham RM, Rasmussen SO, Weiss H (2012) Formal subdivision of the Holocene series/epoch: a discussion paper by a working group of INTIMATE (integration of ice-core, marine and terrestrial records) and the subcommission on quaternary stratigraphy (International Commission on Stratigraphy). J Quat Sci 27:649–659. https://doi.org/10.1002/jqs.2565

Wegmann M, Gudmundsson GH, Haeberli W (1998) Permafrost changes in rock walls and the retreat of alpine glaciers: a thermal modelling approach. Permafr Periglac Process 9:23–33

Zerathe S, Lebourg T, Braucher R, Bourlès D (2014) Mid-Holocene cluster of large-scale landslides revealed in the Southwestern Alps by 36Cl dating. Insight on an Alpine-scale landslide activity. Quat Sci Rev 90:106–127. https://doi.org/10.1016/j.quascirev.2014.02.015

Zoller H, Schindler C, Röthlisberger F (1966) Postglaziale gletscherstande und klimaschwankungen im Gotthardmassiv und Vorderheingebiet. Sonderabdruck aus Verhandl Naturf Ges Basel 77:97–164

X. Gallach (✉) · **L. Ravanel** · **P. Deline**
EDYTEM Laboratory,
Université Savoie Mont Blanc – CNRS,
Le Bourget du Lac, France
Email: xavi.gallach@univ-smb.fr

X. Gallach · **J. Carcaillet**
ISTerre Laboratory,
Université Grenoble Alpes – CNRS,
Grenoble, France

L. Ravanel · **M. Egli** · **D. Brandova** · **M. Schaepman**
Department of Geography,
University of Zurich,
Zurich, Switzerland

M. Christl
Laboratory of Ion Beam Physics, ETH Zürich,
Zurich, Switzerland

S. Gruber
Department of Geography and Environmental Studies,
Carleton University,
Ottawa, Canada

F. Pallandre
ENSA,
Chamonix, France